

# Fan Response to Boundary-Layer Ingesting Inlet Distortions

James E. Giuliani\* and Jen-Ping Chen†  
The Ohio State University, Columbus, Ohio 43210

DOI: 10.2514/1.J054762

The modeling capabilities of TURBO, an existing turbomachinery analysis code, have been extended to include the ability to solve the external and internal flow fields of a boundary-layer ingesting inlet. Flow solutions are presented and compared with experimental data for several high-Reynolds-number flows to validate the solver modifications. The upstream flowfield was coupled to a hypothetical compressor fan to present a fully developed distortion to the fan. Although the total pressure distortion upstream of the fan was symmetrical for this geometry, the pressure rise generated by the fan blades was not, because of the velocity nonuniformity of the distortion. Total pressure profiles at various axial locations are computed to identify the overall distortion pattern, how the distortion evolves through the blade passages and mixes out downstream of the blades, and where any critical performance concerns might be. Stall cells are identified that are stationary in the absolute frame and are fixed to the inlet distortion. Flow paths around the blades are examined to study the stall mechanism. Rather than a typical airfoil stall, it is observed that the nonuniform pressure loading in the radial direction promotes a three-dimensional dynamic stall. The stall occurs at a point of rapid incidence angle oscillation observed when a blade passes through a distortion and re-attaches when the blade sees more uniform flow outside the distortion.

## Nomenclature

$A$	=	amplitude of oscillation
$A_c$	=	inlet capture area
$A_i$	=	inlet throat area
$A_o$	=	inlet mass-flow streamtube area at freestream conditions
$a_{\text{ref}}$	=	reference velocity, km/s
$c$	=	blade chord
$D_2$	=	diameter of the inlet at the aerodynamic interface plane
$I_{\text{LeadingEdge}}$	=	integrated value of total pressure curve at specific span location; blade leading edge
$I_{\text{TrailingEdge}}$	=	integrated value of total pressure curve at specific span location; blade trailing edge
$i$	=	axial cell index
$j$	=	radial cell index
$k$	=	circumferential cell index
$l_{\text{ref}}$	=	reference length, m
$M_\infty$	=	tunnel/external Mach number
$\dot{m}_{2c}$	=	corrected mass flow at the aerodynamic interface plane, kg/s
$P_{t,\infty}$	=	tunnel/external total pressure
$P_{t,i}$	=	total pressure, averaged at a specific $\theta$ location, over 1 fan revolution
$\bar{P}_{t,i}$	=	averaged total pressure, at a specific $\theta$ location, normalized
$\bar{P}_{t,180}$	=	total pressure, averaged at the 180° location, over 1 fan revolution
$q$	=	numerical solution vector
$q_{cl}$	=	solution at centerline point
$Re$	=	Reynolds number
$Re/FT$	=	Reynolds number per foot, 1/ft
$T_{t,\infty}$	=	tunnel/external total temperature
$U$	=	circumferential velocity of the fan at a given radius

$V_x$	=	axial velocity
$V_\theta$	=	relative circumferential velocity
$W_u$	=	absolute circumferential flow velocity
$X_{\text{blade}}$	=	blade length in axial direction
$\alpha$	=	incidence angle, deg
$\beta$	=	blade angle, deg
$\Omega$	=	rotational speed of the fan, RPM
$\delta$	=	flow angle, deg

## I. Introduction

PREVIOUS studies [1,2] have shown that efficiency benefits of propulsion systems that ingest significant amounts of boundary layer are sensitive to the magnitude of duct and compressor losses. Seven categories of physical phenomena were classified as having an impact on the benefits of boundary-layer ingesting (BLI) inlets [2]. These included the state of the boundary layer entering the inlet, the inlet design, evolution of the flow in the inlet, distortion transfer across the fan, response of the fan to the distortion, evolution of the flow downstream of the fan, and duct losses. Current engine installations that divert or bleed off the boundary layer entering the inlet are designed to operate over a wide range of operating conditions and angles of attack. BLI designs will need to meet or exceed these operating parameters, and the boundary layer entering the inlet can be significantly impacted by off-design operating conditions.

Numerous numerical and experimental studies have been performed to analyze the impact that inlet distortion has on the compressor system. Several efforts have approached the problem by modeling individual components with appropriate boundary conditions [3–6]. Recently, work has been published in which solutions of the entire flow field, including both inlet and fan [7,8], have been undertaken in an effort to improve the accuracy of the distortion calculation and its transfer to the fan. Results indicate that there are nonsymmetrical aspects of the inlet distortion that impact the way the fan processes the distortion. Full 3D simulations of the full flowfield are important at this time to identify what flow field phenomena can be modeled with approximations and which require full modeling.

The primary goal of this effort is to develop the TURBO code [9] as a design and analysis tool for accurate prediction of fan response to the nonuniform flow fields generated by BLI inlets. The TURBO code was selected as the base for the model so that the wealth of experience and anchoring of the code to turbomachinery applications can be used to provide increased confidence in the computations of the fan/compressor flow field. The numerical scheme has many of the capabilities to model the coupled inlet/fan flow field and was extended to model the upstream flow in addition to the fan section.

Received 21 September 2015; revision received 4 March 2016; accepted for publication 17 March 2016; published online 30 May 2016. Copyright © 2016 by the American Institute of Aeronautics and Astronautics, Inc. All rights reserved. Copies of this paper may be made for personal and internal use, on condition that the copier pay the per-copy fee to the Copyright Clearance Center (CCC). All requests for copying and permission to reprint should be submitted to CCC at [www.copyright.com](http://www.copyright.com); employ the ISSN 0001-1452 (print) or 1533-385X (online) to initiate your request.

\*Director of Research Computing, College of Engineering, 201 W. 19th Ave. Member AIAA.

†Associate Professor, Mechanical and Aerospace Engineering Dept., 201 W. 19th Ave. Senior Member AIAA.

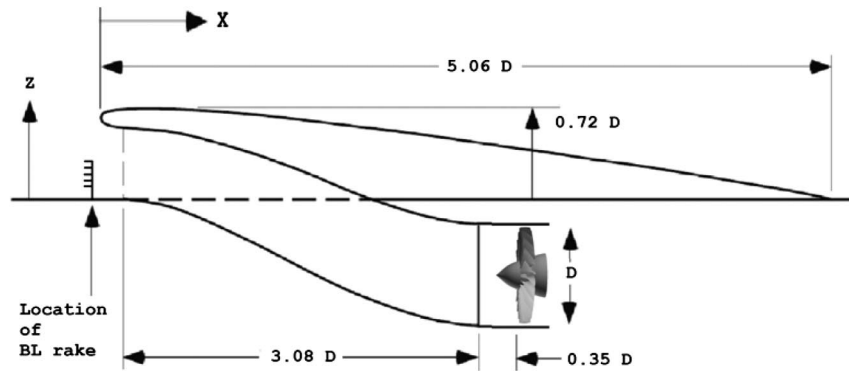


Fig. 1 Geometry of inlet and fan with dimensions relative to AIP diameter ( $D$ ).

Validating the upstream predictive capabilities of the modified code was considered important for future design and analysis projects, and the first phase of the project was to model an inlet-only geometry. To provide experimental data for validation, a BLI inlet geometry [10] from the Blended Wing Body program was modeled with the modified TURBO and numerical results compared with experimental data [11].

This analysis validated the upstream and inlet modifications. To test a fully coupled simulation, the inlet geometry was coupled with a candidate fan to simulate the entire BLI/fan system. Unsteady simulations showed that the sliding interface boundary condition in TURBO accurately transferred the distortion, which for this geometry showed moderate differences from a sinusoidal 1/rev total pressure boundary condition [3–6]. This boundary condition, typically used in engine-only simulations, uses a sinusoidal function to distribute total pressure around the circumference of the inlet. In addition to lower total pressure, the computed distortion is characterized by lower axial velocity and vortical swirls, which result in increased blade loading in the distortion region. Detailed analysis of the flow through the fan shows that the increased total pressure generated by the blades in the distortion region acts to compensate for the low total pressure distortion. Toward the stall limit of the operating range, the increased blade loading can lead to localized blade stall. The stall, caused by the increased incidence angle in the distortion region, stays anchored to the distortion region.

## II. Numerical Model

The TURBO program is a physics-based simulation tool for multistage turbomachinery. The solver computes the fluid conservation laws without ad hoc modeling of any flow phenomenon other than models required for turbulence. This code solves the unsteady Reynolds-averaged Navier–Stokes equations and a decoupled  $k$ - $\epsilon$  turbulence model. The code is implemented in a portable, scalable form for distributed-memory parallel computers using message passing interface (MPI). The parallel implementation employs domain decomposition and supports general multiblock grids with arbitrary grid–block connectivity. The solution algorithm is a Newton iterative implicit time-accurate scheme with characteristics-based finite-volume spatial discretization. The Newton subiterations are solved using a concurrent block–Jacobi symmetric Gauss–Seidel (BJ-SGS) relaxation scheme. Because all of the fundamental fluid mechanics are computed, the code is capable of capturing the nonlinear characteristics of the flow fields of interest. With the actual modeling of blade rows in relative motion, this code is capable of computing the unsteady interactions between blade rows.

### A. Geometry and Operating Conditions

To validate code modifications needed for modeling the inlet geometry, experimental data were needed to compare against numerical results. Several BLI inlet designs, tested in the NASA Langley Research Center 0.3 m Cryogenic Wind Tunnel [12] to evaluate possible geometries for blended-wing-body (BWB) designs [13], were selected. These runs, which attempt to simulate realistic Reynolds numbers of a BWB design at cruise, were selected because of

well-developed distortions observed at the aerodynamic interface plane (AIP). The inlet was a flush-mounted S-duct design with large amounts of boundary-layer ingestion, and the inlet geometry can be seen in Fig. 1, which also shows the fan attached to the inlet for the second phase of the project. Experimental results include total pressure measurements from a fixed rake at the AIP, which represents the attachment point of the fan, static pressure measurements along the tunnel and inlet walls, and a boundary-layer rake. The Inlet A geometry was selected to be modeled, which represents a more conservative lip thickness and semicircular throat aperture.

Although Inlet A provided several test cases with well-developed distortions, no fan was designed and attached to this geometry. A candidate fan model was selected to be scaled down and attached to the numerical Inlet A model to confirm TURBO's ability to simulate a coupled system. The fan geometry selected was a design used at NASA Glenn for aeroacoustic testing (SDT2-R4) and has 22 blades [14]. The combined inlet and fan geometry can be seen in Fig. 1 with dimensions provided relative to the diameter at the AIP. To leverage the known distortions generated by the Inlet A geometry, the SDT2-R4 fan was reduced in scale by a factor of 9.122 to match the Inlet A diameter. With the reduction in fan diameter, an increase in fan rotational speed was required to match the same SDT2-R4 relative flow angles. A fan RPM of 45,000 was selected to match relative incidence angles near the 80% span location.

The inlet flow conditions selected for this analysis were at an external Mach of 0.402 and 0.805. Table 1 provides operating conditions for these cases. To examine the performance of the compressor fan, a speedline was generated for the  $M_\infty = 0.402$  case over the range of  $\dot{m}_{2c}$  from 0.32 to 0.42 kg/s.

### B. Numerical Model

Most turbomachinery applications are axisymmetric about the longitudinal axis. TURBO development has paralleled this and most of the boundary conditions and user input parameters are geared toward axisymmetric geometries. Some modeling efforts [15] have employed independent grids for the fixed upstream inlet flowfield and the rotating grid of the fan section. A transfer mechanism was employed to interpolate and pass data between the two surfaces. For this effort, grids with the same concentric rings at the AIP interface were developed. This allowed the sliding interface boundary condition in TURBO to be used. This proven method maintains continuity at the interface between the fixed and rotating grids.

Choosing to match the grids at the AIP interface complicates meshing the upstream flowfield. An optimal concentric mesh was selected for the fan, and the mesh at the AIP was fixed at this location

Table 1 Target operating conditions for external flow

$M_\infty = 0.402$	$M_\infty = 0.805$
$Re/FT = 52.03 \times 10^6$	$Re/FT = 69.97 \times 10^6$
$T_{t,\infty} = 100^\circ \text{ K}$	$T_{t,\infty} = 100^\circ \text{ K}$
$P_{t,\infty} = 434,370 \text{ Pa}$	$P_{t,\infty} = 351,632 \text{ Pa}$
$\dot{m}_{2c} = 0.4064 \text{ kg/s}$	$\dot{m}_{2c} = 0.4095 \text{ kg/s}$

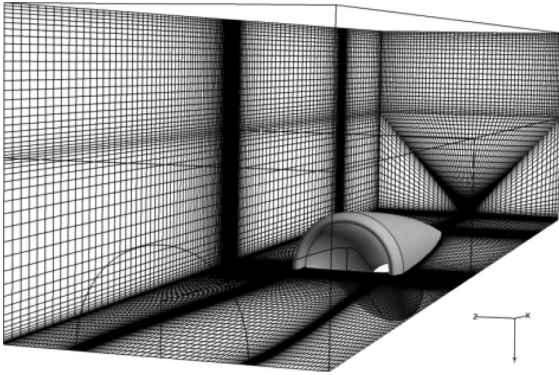


Fig. 2 Numerical mesh of test section and inlet.

and smoothed upstream to fit to the inlet and external geometry. Figure 2 shows the overall model, which represents the complete test section from the experiment. Grid density is shown for the external region of the flow field, whereas the inlet is shown as solid surfaces for clarity. The mesh contains a total of 31 million cells: 10 million cells in the external flow, 2 million cells in the inlet section, and 19 million cells in the full annulus rotor section.

Figure 3 shows the mesh sections from Fig. 2 that contains the inlet mesh and shows how it was extended upstream from the AIP. The concentric grid that is optimal for the fan section can be seen at the AIP and the centerline point is diagramed in Fig. 4. This is an optimal mesh for the rotating section and the inlet near the AIP, and maintains direct connectivity between the inlet and the fan sections. In Fig. 3, only half of the grid elements are displayed, to improve the visual quality.

A new boundary condition was created to handle the singularity at the centerline in the inlet and upstream flowfield in Fig. 3. In a finite difference methodology, the flow properties at the centerline node would be set to the same value, but the finite volume formulation of TURBO is cell centered and flow properties cannot be specified at the

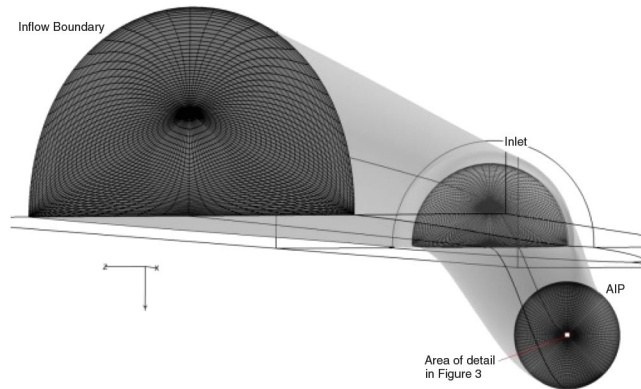


Fig. 3 Mesh sections that include centerline boundary condition.

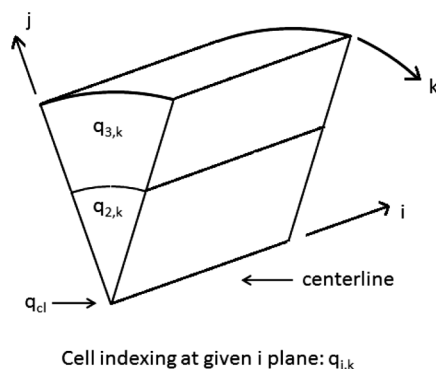


Fig. 4 Schematic of finite volume element at the centerline boundary.

centerline point, point  $q_{cl}$ , in Fig. 4. On all cells that are adjacent to the centerline, the face that lies on the centerline is collapsed and has an area of zero. This prohibits any flux from passing through that face into the cell directly across the centerline. At each  $i$  index, the new centerline boundary condition sets the value of each cell adjacent to the centerline,  $q_{2,k}$ , so that  $q_{cl}$  would be the same for each element. The target value of point  $q_{cl}$  is set to the average of all of the elements surrounding the centerline.

$$q_{cl} = \frac{\sum_{k=2}^{nk} q_{2,k}}{nk - 1} \quad (1)$$

$$q_{2,k} = \frac{2}{3} q_{cl} + \frac{1}{3} q_{\beta,k} \quad (2)$$

A first-order extrapolation is used to determine what the cell-centered values of  $q_{2,k}$  should be to achieve the uniform condition of the target centerline point  $q_{cl}$ . Based on this value of  $q_{cl}$  and the 2nd radial element,  $q_{3,k}$ , an updated value of  $q_{2,k}$  is computed from Eq. (2). The new value of  $q_{2,k}$  for each cell surrounding the centerline helps communicate flowfield data to elements around the centerline.

### III. Results and Discussion

The first phase of the project was to validate the TURBO modifications. The NASA Inlet A geometry was selected so that results could be validated against experimental data. Time-accurate solutions were computed for the two operating conditions given in Table 1, which represent experimental cases in which inlet distortions were observed. To compare against experimental data, results were computed for static pressure along the tunnel wall, static pressure along the inlet lower wall, the total pressure profile in the boundary layer near the inlet, and the total pressure distributions at the AIP. To compare these datasets, the unsteady numerical results were averaged from 20 data samples obtained after the flow was determined to have reached a steady state.

With the inlet distortion validated for the inlet-only model, the coupled solution was validated by scaling the candidate fan to match the inlet geometry and connecting it to the inlet for the  $M_\infty = 0.402$  case. With the diameter of the fan reduced to match the inlet diameter, the rotational speed was increased to maintain similar incidence angles. A speedline curve for the fan was computed to define the operating envelope for this geometry.  $P_t$  and  $T_t$  results were obtained for the unsteady flow at the four axial locations shown in Fig. 5. Flow properties were examined at these locations to help identify how the flow evolves in the blade passages and the mixing region downstream of the fan.

Starting from an initialized flowfield, each simulation was run for 5–7 revolutions with 200 time steps for a blade to sweep through one blade passage. This resulted in 4400 time steps for a full revolution and a time step of  $1.3e - 4$  s. Observing fixed points near the leading edge or downstream of the fan, large variations in flow properties are seen from the passing blades. To provide quantitative insight,  $P_t$  and  $T_t$  results are averaged from 400 data samples acquired over a  $360^\circ$

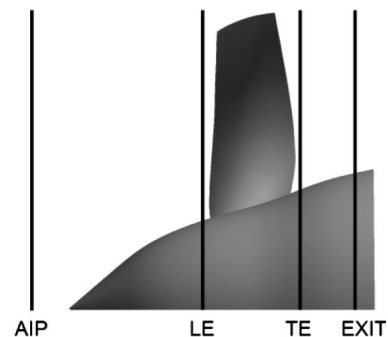


Fig. 5 Axial locations for measuring numerical flow properties.

revolution of the fan. Samples were taken every 11 steps, which provided the largest set of unique sample points. The averaging technique used was a bucket average, with each bucket representing  $1^\circ$ . Every 11 time steps, the flow properties of the grid cells that fall within a bucket are saved. At the end of the simulation, each bucket is averaged by the number of values stored, yielding average values at each degree around the circumference.

### A. External and Inlet Flow Validation

With boundary conditions set to simulate the  $M_\infty = 0.402$  case from Table 1, a solution was obtained that resulted in an external flow velocity of  $M_\infty = 0.403$  in the tunnel section upstream of the inlet. Corrected mass flow at the AIP was computed to be 0.6% higher than the experimental value. Figure 6a shows the Mach number contours at the midplane of the flowfield. With the capture area of the inlet larger than the freestream area of the streamtube, yielding an area ratio of  $A_o/A_c = 0.771$ , some of the external flow bypasses the inlet as spillage and the flow entering the inlet decelerates slightly. The secondary flow structure that evolves in the serpentine inlet, because of the convective derivative term in the vorticity rate of change equation [16], collects the boundary layer on the bottom wall of the duct. The low-momentum region that develops can be seen growing in thickness as the flow progresses axially. The secondary flow migrates the low-momentum fluid up toward the center of the duct and this establishes the distorted flow field at the AIP.

For the experimental case with  $M_\infty = 0.805$ , the numerical solution yielded an external flow of  $M_\infty = 0.770$ , which is about 4.4% lower than the measured freestream Mach number. This difference was a result of having to estimate the static pressure at the external flow outlet, which was not available from the experimental data. Corrected mass flow was computed to be 0.5% over the experimental value. At these operating conditions, the flow in the inlet was found to separate downstream of the inlet entrance. Figure 6b shows Mach contours of the averaged flow field. Some of the unsteadiness can still be seen in the averaged data, but it shows the growth of the low momentum flow along the bottom of the inlet. The low-momentum region at the AIP is thicker for the  $M_\infty = 0.770$  case, compared with the  $M_\infty = 0.403$  case. In Fig. 6b, with an area ratio of  $A_o/A_c = 0.454$ , the flow experiences a greater deceleration as it approaches the inlet compared with Fig. 6a.

Figure 7 compares the experimentally measured normalized static pressure  $P/P_{t,\infty}$  along the bottom of the tunnel wall and the bottom of the inlet, with the time-averaged results. The distance  $x/D_2 = 0$  represents the inlet entrance. Positive values represent axial locations downstream through the serpentine inlet, and negative values represent axial locations upstream of the inlet along the flat external surface. For the  $M_\infty = 0.403$  solution, computed results match well. Far upstream of the inlet, in the range of  $x/D_2 = -8.0$ , the computed pressure is about 0.6% lower than experimental data. This is because the computed external velocity is slightly higher than the experiment. Pressure calculations just downstream of the inlet in the range of  $x/D_2 = 0.5$  report the highest error, differing from experimental values by about 2.5%. The exact cause for this discrepancy was not identified, but results indicate that refinement of the turbulence model

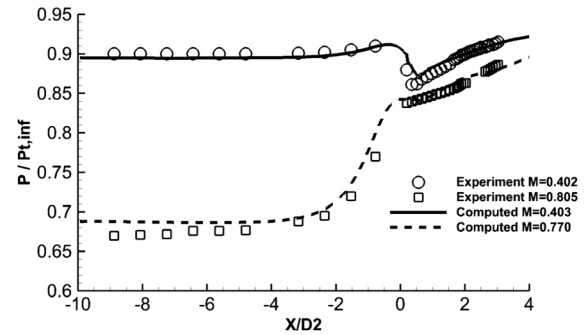


Fig. 7 Normalized static pressure, tunnel and inlet lower wall,  $M_\infty = 0.403$  and  $M_\infty = 0.77$ .

parameters should improve accuracy in this region. Accuracy of the solution improves after the midpoint of the inlet.

In the experiment, the  $M_\infty = 0.805$  case was run over a range of inlet mass flow values. Static wall pressure data for several cases show sudden changes in wall static pressure along the inlet, indicating that this test case is near the transition point between attached and separated flow in the inlet. Mass flow values below the test case show smooth increases in static pressure and mass flow values above the test case show a sharp dip in static pressure just downstream of the inlet. With the computed mass flow within 0.5% of the experimental value, static pressure values predicted downstream of the inlet match well, given that they are averaged. The solution upstream of the inlet, in the range of  $x/D_2 = -8.0$ , overpredicts the static pressure by about 2.5%, due primarily to estimated static pressure at the external outflow boundary.

A boundary-layer rake was employed in the experiment to obtain boundary-layer profile information near the inlet as shown in Fig. 1. The boundary-layer rake was located at the same axial location as the inlet entrance,  $x/D_2 = 0$ , and was offset to the side of the inlet, to avoid disturbing flow entering the inlet. Figure 8 presents the experimental boundary-layer profile along with the computed results. For the  $M_\infty = 0.403$  case, results show that the boundary-layer thickness, as measured by the distance from the wall where  $P_{t,BL}/P_{t,\infty}$  approaches 1, is computed to be approximately  $Y/D_2 = 0.25$ , which is the value measured in the experiment. The total pressure profile within the boundary layer, however, from  $Y/D_2 = 0.0$  to  $Y/D_2 = 0.2$  is not fully captured. The  $y^+$  values for this mesh are in the range of 30 to 100, representing a coarser mesh. The results from the  $M_\infty = 0.770$  case indicate a similar trend. Observations indicate that establishing, at the inlet, the correct distance from the wall at which the total pressure recovers is the primary factor in obtaining a realistic distortion at the AIP. This can be accomplished by setting the inflow boundary far upstream of the inlet and allowing the BL to develop, or moving it closer to the inlet and applying an approximate inflow boundary profile such that the BL still develops in the shorter distance. This observation will be further clarified.

The accuracy of the solution at the AIP is of primary interest without the fan attached, as significant experimental data exist at this plane. Figure 9a shows the normalized total pressure measured at the

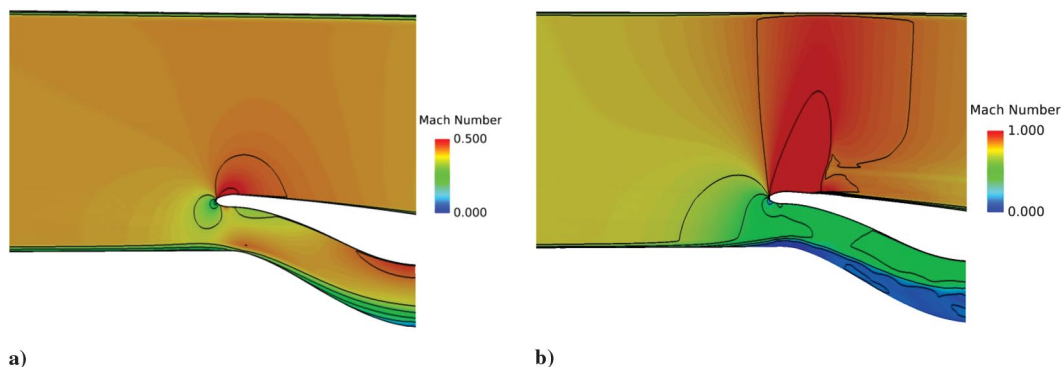


Fig. 6 a) Mach contours, computed  $M_\infty = 0.403$ . b) Mach contours, computed  $M_\infty = 0.770$ .



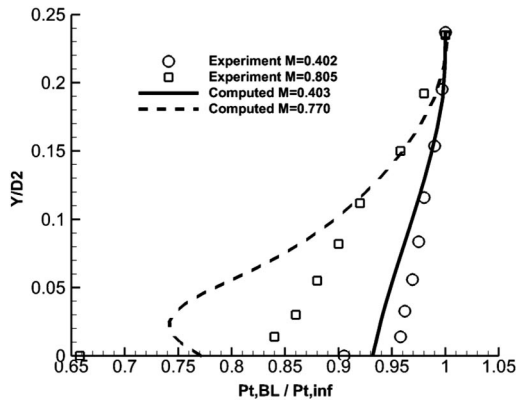


Fig. 8 Normalized total pressure profile from the wall, at entrance to inlet, external velocity  $M_\infty = 0.403$  and  $M_\infty = 0.77$ .

AIP for the experimental  $M_\infty = 0.402$  case. Figure 10a shows the normalized total pressure measured at the AIP for the experimental  $M_{inf} = 0.805$  case. The small circles represent the location of the total pressure probes in the fixed rake. Figure 9b shows the computed results and the secondary flow structure established by the S-duct geometry. The total pressure distortion matches well with the experimental data, both the overall profile as well as the magnitude. The computed flow field provides a much higher resolution than the experimental results, which are interpolated data based on the 40-point total pressure probe rake. The additional vortex characteristics predicted by the simulation, while matching the overall structure, cannot be confirmed because of the lower resolution of the experimental data.

The total pressure distribution computed at the AIP matches the experimental results well, comparing Figs. 9a and 9b, but the total pressure profiles within the boundary layer seen in Fig. 8 show differences between the computed and experimental results. During the approximately 400 simulations that were executed to build the datasets for this project, observations led to the hypothesis that matching the boundary-layer thickness at the inlet entrance is of primary significance when trying to accurately predict the total pressure distortion at the API. Although qualitative in nature and a detailed test matrix was not devised to fully explore this hypothesis, observations indicate that control parameters that impacted the thickness of the BL entering the inlet had primary influence on the predicted distortion. To evaluate this, the  $M_\infty = 0.403$  case and  $M_\infty = 0.770$  case were sampled at several temporal points that represented different stages of the BL growth, from initial development to thickness beyond that measured in the experimental test cases. Figure 11, similar to Fig. 8 with an enlarged  $P_t$  scale, shows four of these boundary-layer profiles at the inlet, computed at the location of the boundary-layer rake. Case 1 represents a time early in the BL development when  $P_t$  recovery is computed closer to the wall than experimental results. Case 2 through case 4 represent successive times at which the BL continued to develop, with case 4 matching the distance from the wall at which the experiment measured the BL recovered to freestream value. Figure 12 shows the corresponding total pressure distortions observed at the AIP for each case. None of the total pressure profiles in the BL, shown in Fig. 11, match the

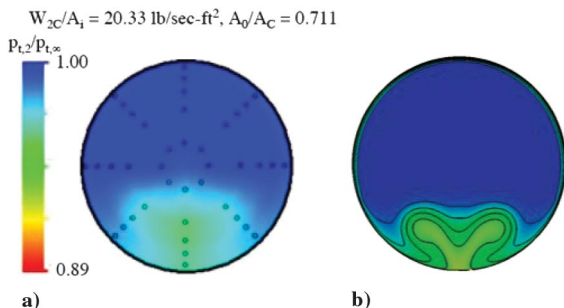


Fig. 9 a) Experimental  $P_t/P_{t,inf}$  at AIP,  $M_\infty = 0.402$ . b) Computed  $P_t/P_{t,inf}$  at AIP,  $M_\infty = 0.403$ .

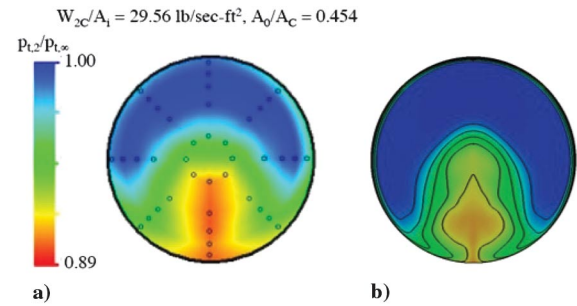


Fig. 10 a) Experimental  $P_t/P_{t,inf}$  at AIP,  $M_\infty = 0.805$ . b) Computed  $P_t/P_{t,inf}$  at AIP,  $M_\infty = 0.770$ .

experimental data exactly, but the distortion predicted at the AIP in Fig. 12 evolves significantly, with case 4 matching the measured profile closely. These qualitative observations indicate a relationship between the upstream boundary-layer thickness, as measured by  $P_t/P_{t,inf}$ , and the total pressure distortion predicted at the AIP. It appears that the distortion depends less on the profile within the boundary layer as all 4 cases observed in Fig. 11 differ from experimental data within the boundary layer, but as the distance from the wall where total pressure recovery approaches the experimentally observed value, prediction of the total pressure distortion at the AIP improves.

Figure 10b shows the total pressure distortion computed for the  $M_\infty = 0.770$  case. The computed distance for  $P_t$  recovery at the inlet entrance for the  $M_\infty = 0.770$  case in Fig. 8 is close to the experimental value, but the value of  $P_t/P_{t,inf}$  within the BL varies more than the lower velocity flow. These data further support the observation that accurately predicting the total pressure boundary-layer thickness is more significant than matching the total pressure profile, as far as the total pressure distortion at the AIP is concerned. Given that the experimental total pressure data were time averaged, it is important to time average the numerical results for the higher-velocity flow because unsteady flow separation was observed in the inlet. Comparing numerical results to the inlet-only experimental data supports the primary purpose of the first phase of this work, which was to validate the behavior of TURBO when modeling the upstream flowfield. The ability of the numerical model to capture the macroscopic properties of the distortion for the  $M_\infty = 0.770$  case, which exhibited flow separation characteristics, documents these capabilities. The effect of the unsteady flow behavior on the coupled inlet/fan solution adds significant uncertainty, and so only the lower velocity  $M_\infty = 0.403$  case is used in the second phase of the project to examine the behavior of the coupled simulation.

## B. Coupled Inlet/Fan Simulation

Results to this point have examined the ability of TURBO to model the inlet-only flowfield of a BLI inlet geometry. The next step was to

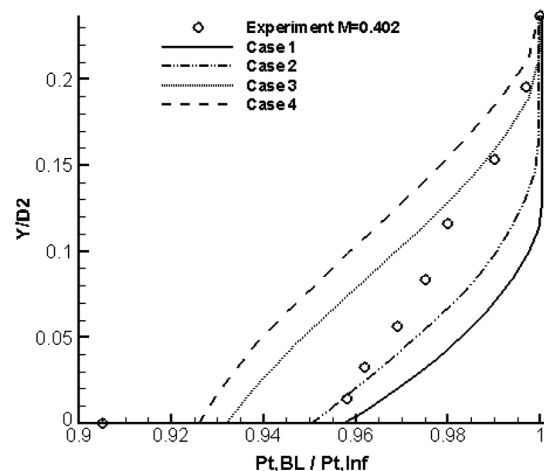
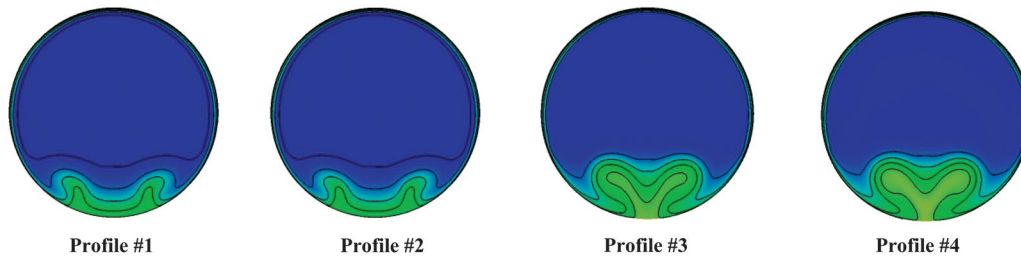


Fig. 11 Evolution of BL  $P_t$  profile development, observed at entrance to inlet, experiment  $M_\infty = 0.402$ , computed  $M_\infty = 0.403$ .



**Fig. 12** Evolution of  $P_t/P_{t,\infty}$  at AIP with four BL profiles at the inlet, all at  $M_\infty = 0.403$ . Profile #4 matches distance from the wall where  $P_t$  recovers to freestream value.

attach a fan to the inlet so that the coupled inlet/fan system could be modeled. Section II.A described the fan geometry that was connected to the fan through the sliding interface in TURBO. As discussed, the fan geometry was scaled to match the geometry of the Inlet A experimental hardware. Although previous simulation data existed for the fan, because the diameter was reduced, design operating conditions for the fan were no longer relevant and hypothetical operating conditions were selected. A fan RPM of 45,000 was selected to match the relative flow angles seen in the actual fan, which rotates at 12,657 RPM.

Figure 13 shows the computed Mach contours for the  $M_\infty = 0.403$  case. Once an initial flowfield was established, four fan revolutions were needed for the unsteady solution to converge. In addition to confirming that the combined model is able to successfully couple the upstream flow to the fan, some qualitative insight is gained into the effect that the fan has on the upstream flowfield for this configuration. Figure 14a shows the total pressure distortion at the AIP computed without the fan, and Fig. 14b shows the distortion computed at the AIP with the fan present. Results in Fig. 14b are time averaged. The distortion can be seen to be reduced in height by a small amount and a small reduction of total pressure loss compared with the inlet-only case can be observed. The secondary flow structure at the AIP, however, is not significantly affected by the presence of the fan for this configuration.

### C. Speedline

With the external flow conditions obtained from the inlet-only solution used as initial conditions, the corrected mass flow at the exit plane of the fan was set to a target mass flow and each solution was allowed to reach pseudo-steady state. The range of corrected mass

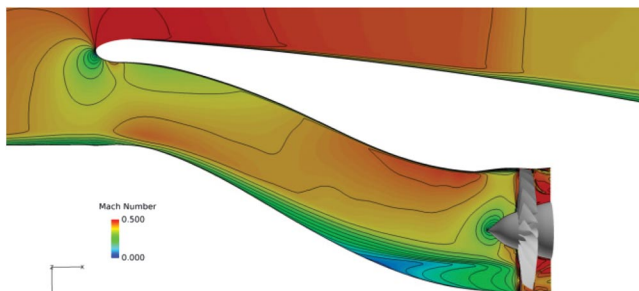


**Fig. 13** Mach number profiles of combined inlet/fan solution,  $M_\infty = 0.403$ .

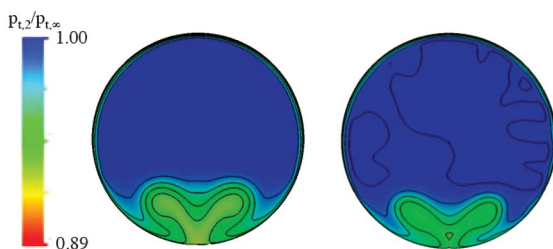


**Fig. 14** a) Computed AIP  $P_t/P_{t,\infty}$  without fan,  $M_\infty = 0.403$ . b) Computed  $P_t/P_{t,\infty}$  with fan,  $M_\infty = 0.403$ .

flow values was extended until solutions diverged and the configuration was assumed to be near the stall or choke limits. Once pseudo-steady state was obtained, the  $P_t$  at the fan exit was averaged and plotted against the corrected mass flow to obtain the speedline curve, shown in Fig. 15. These results confirm the operating envelope for the scaled fan at 45,000 RPM and allow operating points of interest to be identified. The smaller diameter fan and new operating conditions result in a lower pressure ratio compared with the full-size fan operating point, which was 1.47 [14].

### D. Incidence Angle

As observed from the solution without the fan, the inlet distortion presents several flow nonuniformities that the fan must process. In addition to changes in total pressure, variations in axial velocity and swirl upstream of the fan are seen. The nonuniform flow properties will alter the localized work done by the fan blades, resulting in nonuniform work generation and associated pressure rise. The non-uniform pressure rise can act to attenuate or amplify the distortion and the impact on total pressure is of particular interest. In an effort to reduce the upstream velocity characteristics of axial velocity and swirl to one variable for data comparison, incidence angle is examined as a means to capture both axial velocity and swirl effects.

Figure 16a provides a conceptual representation of the cross plane velocity structure observed upstream of the fan. The secondary flow structure that evolves in the serpentine inlet establishes the counter-rotating vortices, labeled A and B, in Fig. 16a. The counterrotating vortices lift the lower momentum fluid that develops near the wall up into the center of the duct, giving the distortion the characteristic of having lower axial velocity than the bulk flow. The lower axial velocity  $u_x$  will increase the change in circumferential velocity imparted by the blade, which increases work input to the flow. A corresponding increase in incidence angle is seen as a result of the lower axial velocity. Swirl upstream of the fan also effects blade loading and incidence angle. No inlet guide vanes are modeled, but the distortion does generate two vortices diagramed in Fig. 16a. Figure 16b shows how vortex A near the wall generates co-swirl that causes a reduction incidence angle and a subsequent decrease in loading. Figure 16c shows how the circumferential flow near the wall,  $u_B$ , of vortex B generates counter-swirl relative to the direction of

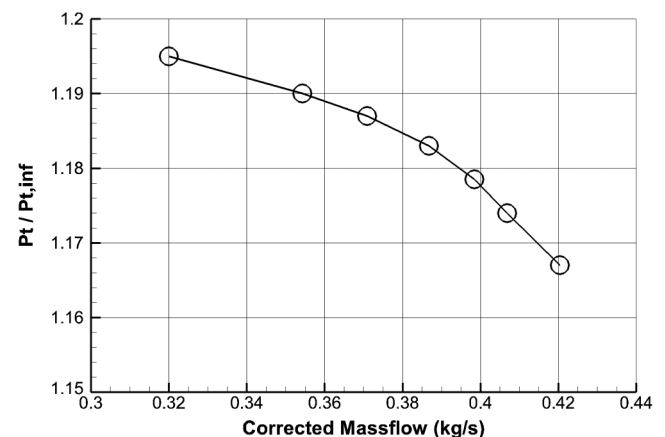


**Fig. 15** Speedline curve for coupled inlet/fan at  $M_\infty = 0.403$ .

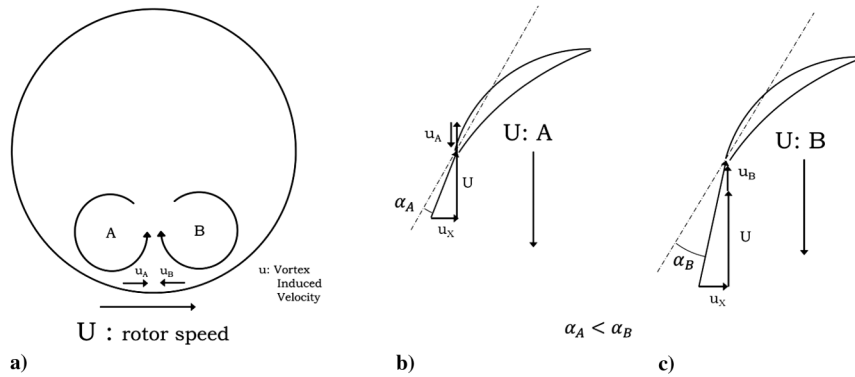


Fig. 16 a) Observed distortion vortices and swirl pattern. b) Velocity triangle for vortex A. c) Velocity triangle for vortex B.

fan rotation, which causes an increase in incidence angle and a subsequent increase in blade loading. Observing incidence angle also provides insight into potential regions of blade stall.

To examine the incidence angle variation caused by the inlet distortion, numerical data were extracted at the three radial locations shown in Fig. 17: 50% span, 70% span, and 80% span. Figure 17

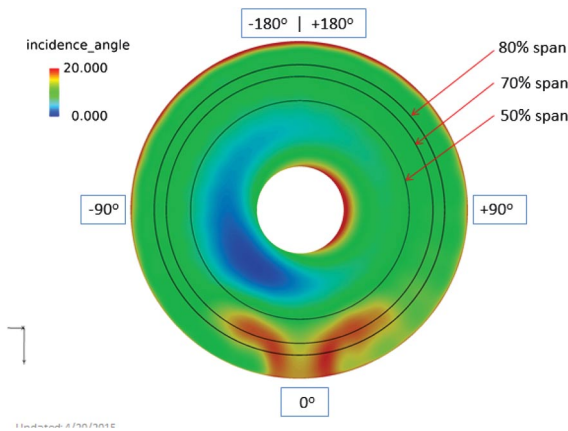


Fig. 17 Incidence angle at  $\dot{m}_{2c} = 0.35$  kg/s.

displays a contour plot of the computed incidence angle distribution just upstream of the fan for the  $\dot{m}_{2c} = 0.35$  kg/s case, which from Fig. 15 can be seen to be toward the stall limit. Figure 18 plots the incidence angle at the 70% span location for three different flow rates. As the flow rate increases, the axial velocity increases and a reduction in incidence angle around the circumference is seen. The counter-rotating vortices generated by the distortion each add a component to the relative circumferential velocity, which can either increase or decrease the incidence angle as explained previously. This highlights an important observation: while the bulk axial velocity deficit from the distortion creates an increase in incidence angle that is symmetrical about the  $0^\circ$  mark, the two counter-rotating vortices introduce a nonsymmetrical incidence angle that results in blade loading that is not symmetrical about the  $0^\circ$  mark.

Several important characteristics of the inlet flow distortion can be seen more clearly in Fig. 19, which plots computed incidence angle at the three span locations shown in Fig. 17 for the  $\dot{m}_{2c} = 0.35$  kg/s case. First, the distortion is not a pure sinusoidal distribution as is often used in numerical studies when the inlet is not modeled [3,6]. For all cases examined, there is an increase in incidence as the first vortex (A) is encountered, followed by a decrease between the vortices and then another increase as the second vortex (B) is encountered. A drop in incidence angle of  $4^\circ$  can be seen for the 80% and 70% radial locations, and a drop of  $2^\circ$  can be seen at the 50% radial location. Although the incidence angle within the distortion for all

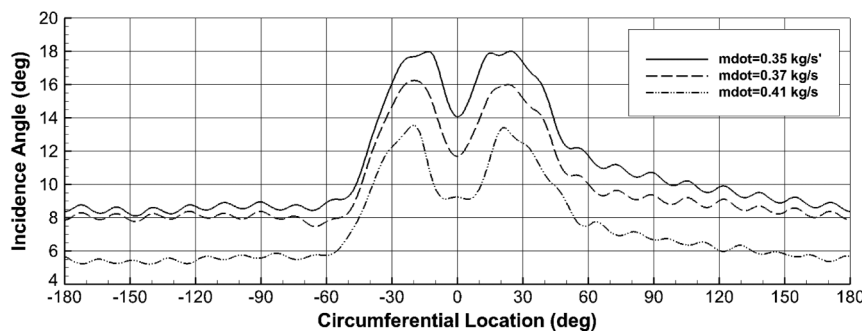


Fig. 18 Incidence angle upstream of fan leading edge,  $M_\infty = 0.403$ .

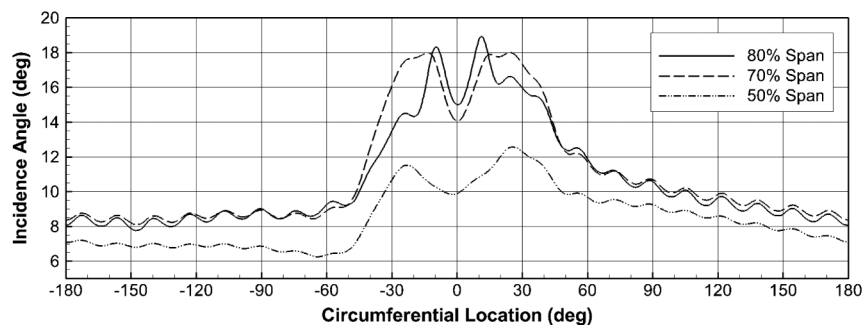


Fig. 19 Incidence angle upstream of fan leading edge;  $\dot{m}_{2c} = 0.35$  kg/s.

cases covers approximately  $100^\circ$ , from  $-50^\circ$  to  $+50^\circ$ , the rates of increase and decrease differ significantly between the three spans. The distortion at 70% span rises to its peak quickly and then remains at the peak until the drop at  $0^\circ$ . At 80% it increases at a lower rate, but then spikes to its peak at about  $-15^\circ$ . The impact these characteristics have on the fan will be examined.

#### E. Total Pressure Distortion at 80% Span

Figures 20a–20c present total pressure at the 80% span radius for this configuration, time averaged over one rotation to eliminate blade passing unsteadiness. Each figure contains curves for three corrected mass flow values, to identify trends at different levels of blade loading. The three mass flow values are taken from the speedline curve in Fig. 15 and represent operating points toward stall ( $0.35 \text{ kg/s}$ ), near design ( $0.37 \text{ kg/s}$ ), and toward choke ( $0.41 \text{ kg/s}$ ). Figure 20a provides total pressure profiles of the inlet distortion at the AIP, normalized by the freestream total pressure, and reflect the effect of the axial velocity deficit generated by the BLI inlet distortion. The twin-vortex structure of the distortion produces a total pressure profile that reaches two minimums, which is different from the 1/rev

sinusoidal  $P_t$  distribution [3,6]. At this axial location, the  $P_t$  distortion remains symmetric about the  $0^\circ$  location.

Figure 20b shows the distortion just upstream of the leading edge of the fan blades. The distortion shows some change in the magnitude of the distortion and profile. These are attributed to upstream influence of the fan blades and the decrease in span of the flow passage as a result of the increasing spinner diameter.

Figure 20c shows the  $P_t$  distortion downstream of the fan trailing edge. Several important characteristics are observed. First, whereas there were two distinct minima in the  $P_t$  profile in Fig. 20b, only one minimum can be clearly observed in Fig. 20c, located circumferentially around  $-55^\circ$ . In the two higher flow rate cases, a peak in  $P_t$  is seen at approximately  $+30^\circ$ . The  $\dot{m}_{2c} = 0.35 \text{ kg/s}$  case deviates from the other two cases in this region, where a sharp drop off in  $P_t$  is seen starting at  $+30^\circ$ . The  $P_t$  reaches a minimum around  $+75^\circ$  before increasing and reaching a second peak at  $+90^\circ$ . Because the  $\dot{m}_{2c} = 0.35 \text{ kg/s}$  case experiences the highest loading of the three cases, based on calculated incidence angles, it is believed that this represents a local stalling of the blade and will be examined in more detail.

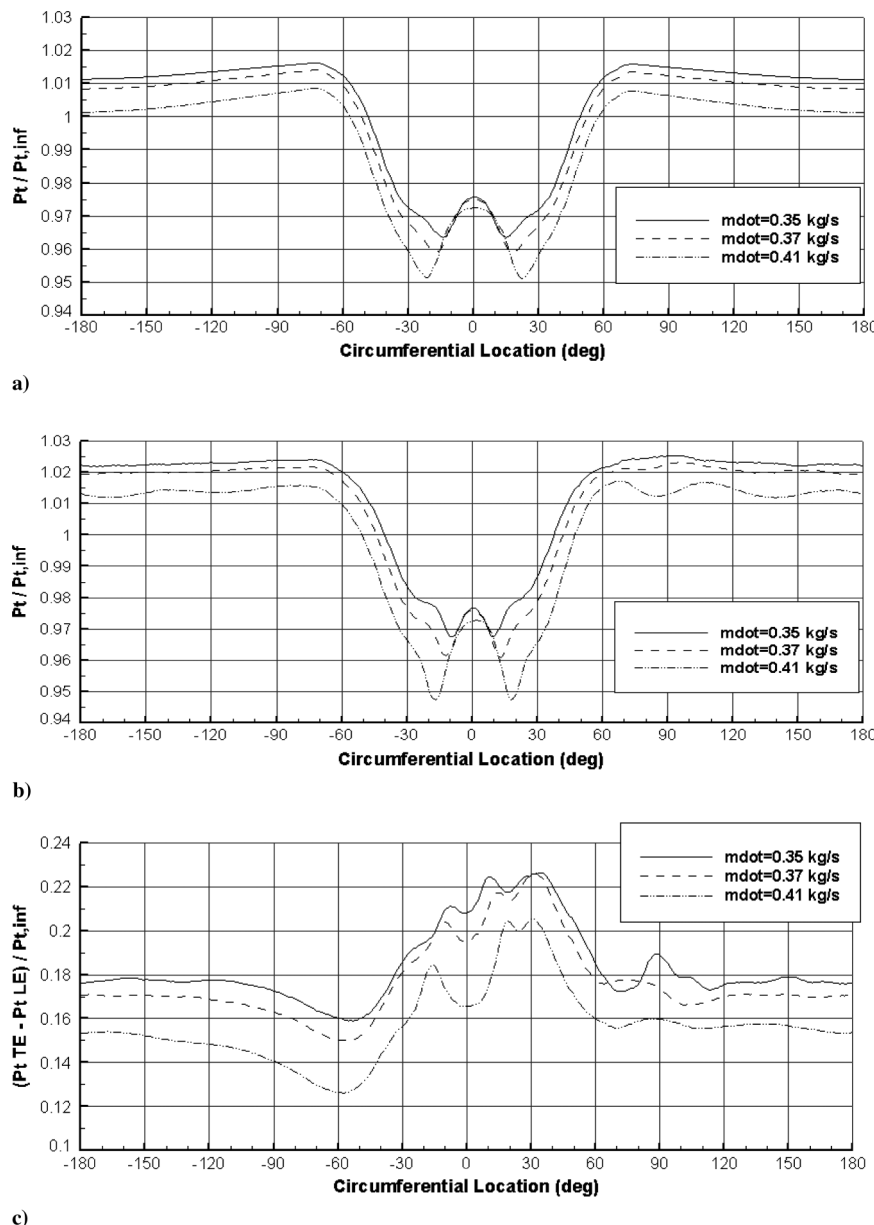


Fig. 20 a) Normalized total pressure at AIP; 80% span. b) Normalized total pressure at leading edge; 80% span. c) Normalized total pressure at trailing edge; 80% span.



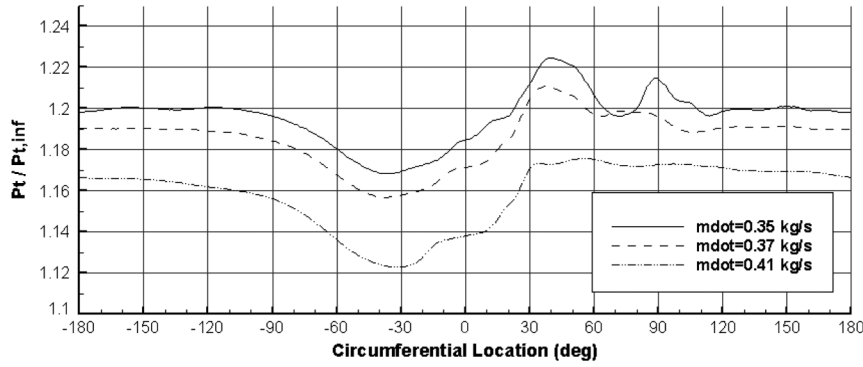


Fig. 21 Delta  $P_t$  between trailing edge and leading edge of the fan.

The nonuniform generation of total pressure, which results from the distortion, can be examined in Fig. 21, which plots the total pressure differential between the trailing edge and the leading edge of the fan. From Fig. 20b, the edge of the distortion can be estimated to occur at  $-65^\circ$ , as the drop in  $P_t$  caused by the distortion can be seen to start at this location. Unlike the symmetrical  $P_t$  distortion upstream of the fan, the  $P_t$  generated is not symmetrical. As the blades pass through vortex A in Fig. 17a, the corresponding  $P_t$  generated can be seen in Fig. 20 in the  $-50^\circ$  to  $0^\circ$  region. Additional  $P_t$  is generated as the blade passes through vortex B in the  $0^\circ$  to  $50^\circ$  range, because of the counter-swirl of vortex B. This trend is seen in both the  $\dot{m}_{2c} = 0.37 \text{ kg/s}$  and  $\dot{m}_{2c} = 0.41 \text{ kg/s}$  cases. In the  $\dot{m}_{2c} = 0.35 \text{ kg/s}$  case, the loss of  $P_t$  generation at the  $+75^\circ$  location is observed as well.

#### F. Total Pressure Attenuation

One of the primary BLI inlet distortion characteristics observed at the AIP is the lower total pressure in the distortion region. For the configuration examined, recovery of some of the total pressure was observed after passing through the fan because of the nonuniform work done as a result of the distortion. An overall total pressure recovery is observed, with some nonsymmetry because of the two vortices imparting co-swirl and counter-swirl. The amount of attenuation depends on many factors, including the initial total pressure deficit, blade geometry, and operating conditions. Understanding how much of the low total pressure distortion is attenuated in different configurations can provide useful design information.

To arrive at an estimate of the distortion attenuation, the averaged total pressure profile at the leading edge is normalized by the averaged total pressure at the  $180^\circ$  circumferential location, and noted  $0^\circ$  represents the bottom of the inlet. The  $180^\circ$  location represents the top of the inlet where flow properties are farthest from the distortion and would be similar to undistorted flow at that axial location. This is then shifted by  $1.0$  so that the undistorted flow corresponds to  $0.0$ .

$$\tilde{P}_{t,i} = \frac{\bar{P}_{t,i}}{\bar{P}_{t,180}} - 1 \quad (3)$$

The resulting curve is shown in Fig. 22. The flow outside of the distortion region has been normalized to zero and the distortion region

shows as negative values. By numerically integrating this curve, the computed area under the curve is a measure of the magnitude of the total pressure distortion. A large negative value would indicate a large distortion, whereas a value close to zero would indicate a minimal distortion. Figure 23 shows the total pressure curves at the trailing edge, with the same normalization applied. An increase in the integrated function relative to the value at the leading edge would indicate some attenuation of the total pressure deficit. This can be used to approximate the total pressure deficit generated by the distortion upstream of the fan and if the deficit grows or diminishes downstream of the fan.

Using the values presented in Figs. 22 and 23 and numerically integrating, the following equations are used to approximate the distortion attenuation:

$$I_{\text{LeadingEdge}} = \frac{1}{2} \sum_{i=1}^N [\overline{(P_{t,LE}(\theta_i) + P_{t,LE}(\theta_{i+1}))}](\theta_{i+1} - \theta_i) \quad (4)$$

$$I_{\text{TrailingEdge}} = \frac{1}{2} \sum_{i=1}^N [\overline{(P_{t,TE}(\theta_i) + P_{t,TE}(\theta_{i+1}))}](\theta_{i+1} - \theta_i) \quad (5)$$

$$\% \text{ Distortion Attenuation} = \frac{I_{\text{TrailingEdge}} - I_{\text{LeadingEdge}}}{|I_{\text{LeadingEdge}}|} \times 100 \quad (6)$$

A 100% distortion attenuation would then indicate that the entire total pressure deficit in Fig. 22 would be balanced by the additional generation in the high blade loading region. For the  $\dot{m}_{2c} = 0.35 \text{ kg/s}$  case, Eq. (6) yields a 80.45% distortion attenuation, or total pressure recovery at the exit of the fan blades. The value for the  $\dot{m}_{2c} = 0.37 \text{ kg/s}$  case is 61.70% and for the  $\dot{m}_{2c} = 0.41 \text{ kg/s}$  case it is 40.52%. This trend matches expectations. The lower mass flow cases represent conditions of lower axial velocity and, therefore, higher incidence angle and blade loading. The higher blade loading in the distortion region generates more total pressure that acts to attenuate

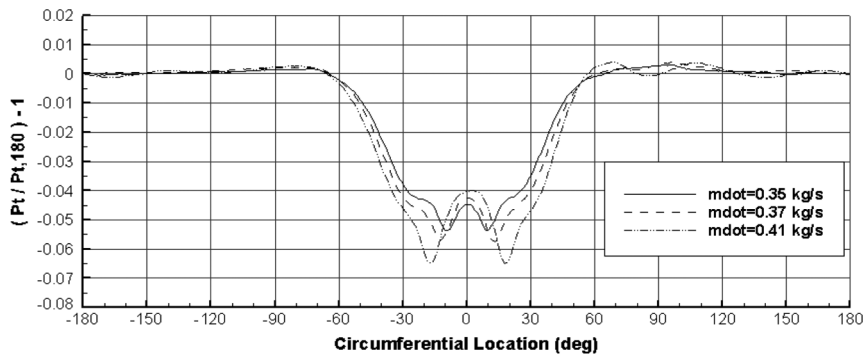


Fig. 22 Normalized  $P_t$  upstream of leading edge.

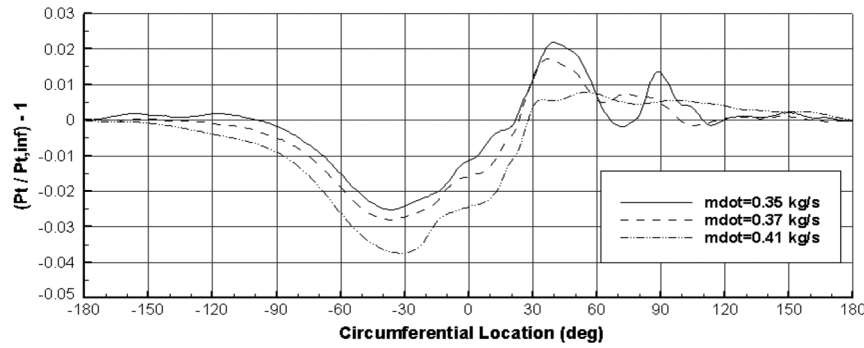


Fig. 23 Normalized  $P_t$  downstream of trailing edge.

more of the initial deficit. As the mass flow increases and blade loading is reduced, less of the total pressure is recovered with the lower blade loading.

### G. Stall Cell

An important observation in Fig. 20c is that there is a sharp drop in  $P_t$  from  $40^\circ$  to  $85^\circ$  in the 0.35 kg/s case, which is not seen at the higher flow rates. With this operating point toward the stall boundary in the speedline curve, there was a high probability that the total pressure loss indicated a blade stall. Since the drop in total pressure appears in results that are averaged, this indicates that the event is stationary relative to the absolute frame.

Streamlines of the flow were examined at the 50, 70, and 80% span locations. In regions outside of the distortion, a pattern similar to that seen in Fig. 24 was observed. The top image shows the blade in its location relative to the distortion with particle streamlines plotted in the relative frame. A color contour is overlaid that shows the incidence angle just upstream of the leading edge. Incidence angles along the span of the blade at this location are largely uniform and particle paths follow the blade contour. The middle image shows the blade oriented with the root to the right and the tip to the left, with a contour plot of pressure mapped to the blade surface. The suction side of the blade is shown and the blue represents lower pressure, and green and yellow higher pressure. The bottom image depicts the relative flow properties observed from the solution data. Loading, represented by pressure on the suction surface at two span locations,  $P_1$  and  $P_2$ , is fairly uniform. In Fig. 24 the flow path denoted by the arrow and labels  $P_1$  and  $\alpha_1$  represent a path near the 70% span location, with path 1 being nearest to the blade tip. The flow path denoted by the arrow and  $P_2$  and  $\alpha_2$  is near the 50% span location. Incidence angles around the circumference at radial locations 50, 70, and 80% of the blade span for the 0.35 kg/s case can be found in Fig. 19. When the blade first enters the distortion, passing from  $-50^\circ$  to  $-25^\circ$ , the incidence angle at each span location increases almost uniformly. The 70% span location sees the most rapid change, increasing  $8^\circ$  over this distance, whereas at 80% and 50% span an increase of  $4^\circ$  is observed in Fig. 19. As the blade continues to travel from  $-25^\circ$  to  $-10^\circ$ , the incidence angle at the 80% span location increases another  $4^\circ$  to reach the same level as the 70% span; however, the 50% span location experiences a drop in incidence of  $4^\circ$ . This represents a significant transition along the span of the blade. Figure 25 shows the blade at a location where it experiences a higher incidence at the 70% span location and a lower incidence at the 50% span location. The higher incidence near path 1 generates more lift, resulting in a low suction surface pressure at station 1. With the flow along path 2 seeing a lower incidence angle, the suction surface pressure along path 2 is higher than that along path 1, which results in a radial pressure gradient pushing flow from the 50% span location toward the 70% span location.

In Fig. 25 the pressure gradient between the 50% and the 70% span locations encourages the flow to turn radially toward the tip of the blade. As  $\alpha_1$  approaches the stall limit, the classic 2D stall pattern [17] is not seen with the 70% span flow. Instead, the lower incidence  $\alpha_2$  flow appears to be pulled under the flow at the 70% span and toward

the blade tip. This flow is then pulled to the tip region where it is entrained in the tip vortex. The flow recovers without full separation and the process repeats as the blade passes through the 2nd vortex in the distortion. As discussed, the 2nd vortex represented by vortex B in Fig. 17a generates counter-swirl near the wall and the blade experiences the highest loading at a circumferential location around  $+25^\circ$ . The higher incidence causes the flow to become unstable and separate briefly. It appears that this separation generates the total pressure loss seen in Fig. 20c at  $70^\circ$ . As the blade passes out of the distortion and the incidence angle drops, the flow reattaches, but some induced oscillation is seen in the tip flow vortex as the blade proceeds through its rotation.

This behavior is similar to the dynamic stall seen in rotor craft and wind turbines [17,18]. For those cases the dynamic stall is predominantly 2D, where flow is mainly in the axial direction, and experiences a classic 2D stall profile. It is characterized by rapid oscillations of incidence angle and one of the effects is a delay in the airfoil stall, beyond the classic stall angle. The flow re-attaches when the angle of

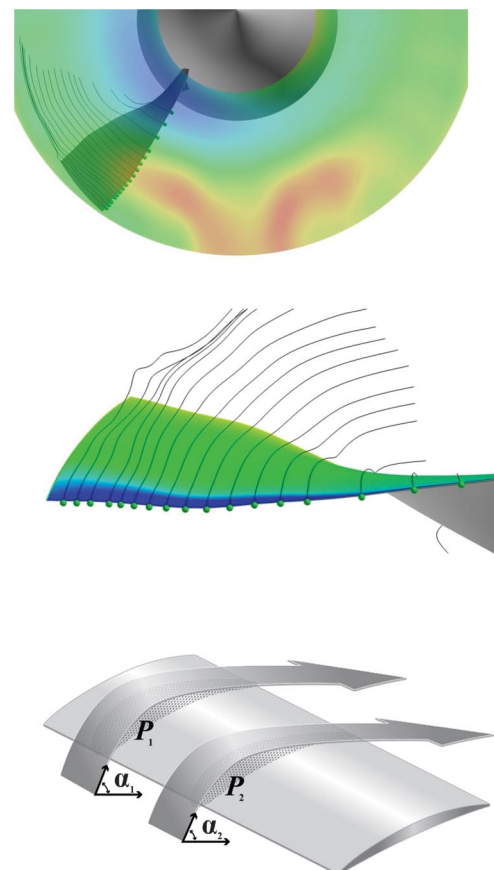
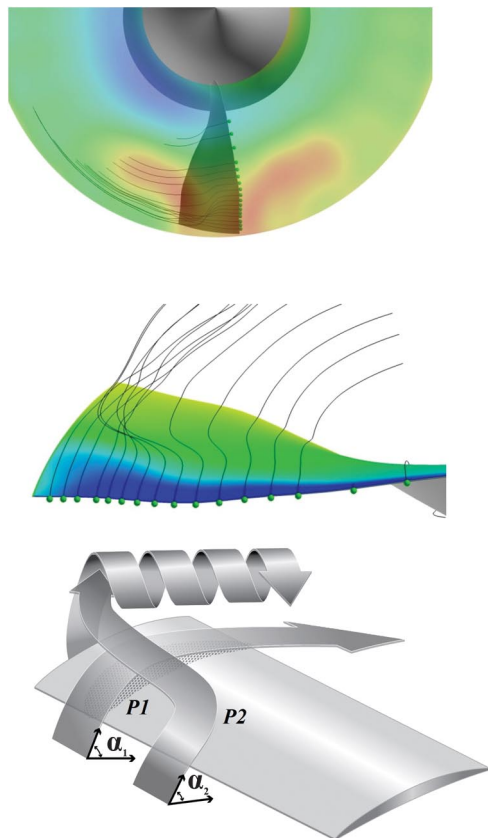


Fig. 24 Incidence angle and flow pathlines at approximately 70% span ( $P_1$ ) and 50% span ( $P_2$ ).  $\alpha_1 \cong \alpha_2$ ;  $P_1 \cong P_2$ .



**Fig. 25 Incidence angle and flow pathlines at approximately 70% span (P1) and 50% span (P2).  $\alpha_1 > \alpha_2$ ;  $P_1 < P_2$ .**

attack decreases as part of the oscillation. In the behavior diagrammed in Fig. 24, 3D effects are seen because of the pressure differential and the variation in incidence angle in the radial direction. Although the sinusoidal 1/rev total pressure profile might approximate the BLI distortion in Fig. 20a on a macroscopic scale, it does not capture the additional blade loading oscillations that the blade experiences. These will have important significance for the blade aeromechanics and potential for triggering dynamic stall.

#### IV. Conclusions

The TURBO extensions for modeling BLI inlets were validated by comparing results to the experimental NASA Inlet A geometry and test results. The secondary flow field structure that develops in the inlet was successfully modeled for external velocities of  $M_\infty = 0.402$  and  $M_\infty = 0.805$ . Numerical results of tunnel wall and inlet wall static pressure showed good agreement with experimental data. Total pressure boundary-layer thickness in the external flow and the corresponding total pressure distortion at the AIP were examined for several boundary-layer profiles. Results indicate that matching the total pressure boundary-layer thickness has the most significant impact on the accuracy of predicting the total pressure distortion at the AIP.

A candidate fan was selected to attach to the inlet so that a coupled inlet/fan system could be modeled and operated at conditions from the  $M_\infty = 0.402$  case. Unsteady simulations showed that the distortion at the AIP experiences a small reduction in height along with a reduction of total pressure loss, but overall the secondary flow structure experiences minimal effect by the presence of the fan for the chosen configuration. To examine the response of the fan, the total pressure was extracted at points around the circumference and averaged over one revolution. Total pressure profiles were compared at three corrected mass flows. Higher total pressure generation was

seen at lower mass flows, because of higher blade loading. Blade loading was not uniform because of the inlet distortion.

The nonuniform blade loading was observed to generate additional total pressure in the distortion region, attenuating the distortion by generating total pressure recovery. An equation to estimate the amount of distortion attenuation was developed and applied to three engine flow rates. Lower flow rates experienced the highest total pressure generation in the distortion region, relative to the bulk flow, and exhibited the highest attenuation of the total pressure deficit. Higher flow rates experienced less total pressure generation in the distortion region and correspondingly less of the total pressure deficit was recovered.

Finally, flow streamlines were examined to search for the cause of an hypothesized blade stall in the highest loading case. Flow behavior similar to dynamic stall was observed as the blades pass through each vortex that makes up the larger distortion region. The first vortex, which generates smaller incidences, caused flow disruption, but did not cause flow separation. As the blade passed through the 2nd vortex, which generates larger incidences, separation was observed and the stall cell appears stationary in the absolute frame relative to the inlet distortion and does not rotate. The flow behavior had strong secondary flow effects and appear coupled to the oscillations in incidence angle. An important observation is that the BLI inlet distortion generates a total pressure distortion that is more complex than the sinusoidal 1/rev total pressure profile commonly used as an inflow boundary condition. The 1/rev sinusoidal distortion would not capture the cyclic blade loading that was observed and will have important significance for the blade aeromechanics and potential for triggering dynamic stall.

#### Acknowledgments

The authors are grateful for the technical discussions provided by Milind Bakhle of NASA Glenn Research Center. This work was supported in part by an allocation of computing time from the Ohio Supercomputer Center under Project PAS0239.

#### References

- [1] Smith, L. H., "Wake Ingestion Propulsion Benefit," *Journal of Propulsion and Power*, Vol. 9, No. 1, 1993, pp. 74–82.
- [2] Plas, A. P., Sargeant, M. A., Crichton, D., Greitzer, E. M., Hynes, T. P., and Hall, C. A., "Performance of a Boundary Layer Ingesting (BLI) Propulsion System," AIAA Paper 2007-450, 2007.
- [3] Yao, J., Gorrell, S. E., and Wadia, A. R., "High-Fidelity Numerical Analysis of Per-Rev-Type Inlet Distortion Transfer in Multistage Fans—Part II: Entire Component Simulation and Investigation," *ASME Journal of Turbomachinery*, Vol. 132, No. 4, May 2010, Paper 041015.
- [4] List, M. G., and Howard, R. M., "Investigation of Total Pressure and Swirl Distortion in a Single-State Transonic Fan," *2012 High Performance Computer Modernization Program Contributions to DoD Mission Success*, Lorton, VA, Sept. 2012, pp. 290–298.
- [5] Herrick, G., "Effects of Inlet Distortion on Aeromechanical Stability of a Forward-Swept High-Speed Fan," *46th AIAA/ASME/SAE/ASEE Joint Propulsion Conference*, AIAA Paper 2010-6711, July 2010.
- [6] Weston, D. B., Gorrell, S. E., and Marshall, M. L., "Analysis of Turbofan Performance Under Total Pressure Distortion at Various Operating Points," *ASME TURBO Expo 2015*, ASME Paper GT2015-42879, June 2015.
- [7] Chima, R. V., Arend, D. J., Castner, R. S., Slater, J. W., and Truax, P. P., "CFD Models of a Serpentine Inlet, Fan, and Nozzle," NASA TM-2010-216349, May 2010.
- [8] Allan, B. G., and Owens, L. R., "Numerical Modeling of Flow Control in a Boundary-Layer-Ingesting Offset Inlet Diffuser at Transonic Mach Numbers," *44th AIAA Aerospace Sciences Meeting*, Reno, NV, 2006.
- [9] Chen, J. P., and Whitfield, D. L., "Navier-Stokes Calculations for the Unsteady Flowfield of Turbomachinery," *AIAA Conference*, AIAA Paper 1993-0676, 1993.
- [10] Berrier, B. L., and Allan, B. G., "Experimental and Computational Evaluation of Flush-Mounted, S-Suct Inlets," *42nd AIAA Aerospace Sciences Meeting*, AIAA Paper 2004-0764, Jan. 2004.
- [11] Giuliani, J. E., Chen, J. P., Beach, T., and Bakhle, M., "Numerical Simulation of Boundary Layer Ingesting (BLI) Inlet/Fan Interaction," *50th AIAA/ASME/SAE/ASEE Joint Propulsion Conference*, AIAA Paper 2014-3731, July 2014.

- [12] Mineck, R. E., and Hill, A. S., "Calibration of the 13- by 13-Inch Adaptive Wall Test Section for the Langley 0.3-Meter Transonic Cryogenic Tunnel," NASA Technical Paper 3049, Dec. 1990.
- [13] Berrier, B. L., Carter, M. B., and Allan, B. G., "High Reynolds Number Investigation of a Flush-Mounted, S-Duct Inlet with Large Amounts of Boundary Layer Ingestion," NASA Technical Paper 2005-213766, Sept. 2005.
- [14] Woodward, R. P., and Hughes, C. E., "Noise Benefits of Increased Fan Bypass Nozzle Area," NASA TM-2004-213396, Nov. 2004.
- [15] Webster, R. S., Sreenivas, K., Hyams, D. G., Hilbert, C. B., Briely, W. R., and Whitfield, D. L., "Demonstration of Sub-System Level Simulations: A Coupled Inlet and Turbofan Stage," *AIAA/ASME/SAE/ASE Joint Propulsion Conference*, AIAA Paper 2012-4282, 2012.
- [16] Greitzer, E. M., Tan, C. S., and Graf, M. B., *Internal Flow: Concepts and Applications*, Cambridge Univ. Press, Cambridge, England, U.K., 2004, pp. 1–23.
- [17] Ekaterinaris, J. A., and Platzer, M. F., "Computational Prediction of Airfoil Dynamic Stall," *Progress in Aerospace Sciences*, Vol. 33, Nos. 11–12, April 1998, pp. 759–846.
- [18] Visbal, M. R., and Shang, J. S., "Investigation of the Flow Structure Around a Rapidly Pitching Airfoil," *AIAA Journal*, Vol. 27, No. 8, Aug. 1989, pp. 1044–1051.

S. Fu  
Associate Editor